Selective layer-free blood serum ionogram based on ion-specific interactions with a nanotransistor

Sivakumarasamy, R.; Hartkamp, R.; Siboulet, Bertrand; Dufrêche, Jean François; Nishiguchi, K.; Fujiwara, A; Clément, N.

DOI
10.1038/s41563-017-0016-y

Publication date
2018

Document Version
Final published version

Published in
Nature Materials

ARTICLES
https://doi.org/10.1038/s41563-017-0016-y
nature materials

Selective layer-free blood serum ionogram based on ion-specific interactions with a nanotransistor

R. Sivakumarasamy[1,5], R. Hartkamp[2,5], B. Siboulet[3], J.-F. Dufrêche[3], K. Nishiguchi[4], A. Fujiwara[4] and N. Clément[1,4*]

Despite being ubiquitous in the fields of chemistry and biology, the ion-specific effects of electrolytes pose major challenges for researchers. A lack of understanding about ion-specific surface interactions has hampered the development and application of materials for (bio-)chemical sensor applications. Here, we show that scaling a silicon nanotransistor sensor down to ~25 nm provides a unique opportunity to understand and exploit ion-specific surface interactions, yielding a surface that is highly sensitive to cations and inert to pH. The unprecedented sensitivity of these devices to Na^+ and divalent ions can be attributed to an overscreening effect via molecular dynamics. The surface potential of multi-ion solutions is well described by the sum of the electrochemical potentials of each cation, enabling selective measurements of a target ion concentration without requiring a selective organic layer. We use these features to construct a blood serum ionogram for Na^+, K^+, Ca^{2+} and Mg^{2+}, in an important step towards the development of a versatile, durable and mobile chemical or blood diagnostic tool.

Tremendous efforts in biointerface science are being made towards engineering biocompatible materials that exhibit specificity, with the aim of understanding biological systems and imparting bioinspired functionality to technological devices[1–3]. However, the limited understanding of ion–surface interactions[4–8], which play a central role in biointerface science, has restricted the development of such materials.

In applications such as coarse-grained biomolecular modelling[9,10] and biosensor simulation software[11–13], ion–surface interactions are often considered solely from the perspective of non-specific electrostatic interactions. By contrast, ion-specific effects are important in modulating the structure and function of biomolecules[14]. These effects are complex to model and are typically assessed by fully atomistic molecular dynamics (MD) simulations[5,6,15]. Although not entirely clear, the mechanisms underlying ion-specific surface effects are strongly related to hydrophilic/hydrophobic surface interactions[5] and site characteristics (conformation and effective charge (Hocine et al., in preparation)). The Hofmeister effect was initially proposed as an ion classification scheme, according to the ability of ions to salt out/in proteins[16]. This effect provides a guide to the preferential adsorption order ($Li^+ > Na^+ > K^+$ for deprotonated metal oxides[6,14]), but the nature of the chemical reactions at the surface remains unclear. For example, some studies suggest a direct adsorption process[6,14,17], whereas others describe pH-mediated adsorption[7,18].

Independent of the selected model or surface type, the Nernst equation is often used to describe the dependence of the surface potential ψ_0 on the log of an ion activity $[i]$[7,13,19]. The site binding model (SBM), which simultaneously considers the Boltzmann ion distribution and changes in surface charge, quantitatively reproduces ψ_0 responses to pH[7,12,13]. The Nernst slope $A_i = \delta\psi_0/\delta\log[i]$ is upper-bounded by the Nernst (or Boltzmann) limit $A_i = kT\ln(10)/z_iq = 59\,\mathrm{mV}$ per $\log[i]$ at room temperature, where k is the Boltzmann constant, T is temperature, z_i is the ion valency and q is the elementary charge. This thermodynamic limit governs the cell membrane potential and the response of batteries or ion sensors. Even if A_i is amplified, for example by capacitive amplification using a coupled capacitor[20], the intrinsic Nernst limit will remain for ψ_0. Shklovskii and colleagues predicted that strong electrostatic correlations between ions (especially multivalent ions) at interfaces could break the Nernst limit[21,22]. The experimentally observed inversion of electrophoretic mobility in biomolecular or nanofluidic systems with added salt is usually attributed to such electrostatic correlations[8,23]. However, how this effect relates to the Nernst limit is not clear, particularly as the ζ potential measured by electrophoretic mobility provides an underestimate of ψ_0[19].

Improved knowledge of ion-specific interactions and ψ_0 could reveal key information regarding electrophoretic mobility[6], enzyme activity[24], protein surface charge[5] and biosensor response[7], and would be of fundamental technological importance. Among possible applications for bioinspired technology, point-of-care diagnosis (bedside testing) has been proposed to improve patient care by allowing quicker decision making[25]. However, the high costs of bedside testing have limited its diffusion (see 'Executive Summary' on page ix of http://www.chumontreal.qc.ca/sites/default/files//documents/A_propos/PDF/analyseur_hors_laboratoirei-stat_dans_les_services_urgence_du_chum.pdf). These costs are related to the lack of versatility and the requirements of biocompatibility, single-use cartridges, labels, and mass fabrication of sensors. One common aspect of these issues relates to the so-called selective layer, which is designed to capture an analyte selectively. Addition of a thin organic selective layer to sense analytes other than H_3O^+ disrupts the high durability and precision of metal oxide -covered miniaturized pH sensor devices[20,26–30]. A fundamentally different approach would be to take advantage of non-covalent specific surface interactions to perform selective-layer-free measurements of analytes in unknown solutions with a versatile and mass-fabrication-compatible device.

Here, we describe insights into ion-surface interactions and demonstrate a selective layer-free blood serum ionogram application

[1]Institute of Electronics, Microelectronics, and Nanotechnology, CNRS, University of Lille, Villeneuve d'Ascq, France. [2]Process and Energy Department, Delft University of Technology, Delft, the Netherlands. [3]Institut de Chimie Separative de Marcoule ICSM, ICSM, CEA, CNRS, ENSCM, Montpellier University, Marcoule, Bagnols-sur-Ceze, France. [4]NTT Basic Research Laboratories, NTT Corporation, Atsugi-shi, Japan. [5]These authors contributed equally: R. Sivakumarasamy, R. Hartkamp. *e-mail: nicolas.clement@lab.ntt.co.jp

for Na^+, K^+, Ca^{2+} and Mg^{2+} using a ~25 nm silicon transistor sensor. The paper is organized as follows. First, we show that our nanoscale device is inert to pH on a wide pH range, eliminating the pH-mediated adsorption process in its simple form. Consistent with MD simulations, we report clear signatures of ion-specific effects for cations, including the Hofmeister effect and sensitivities beyond the Nernst limit. Combining experiments and theory, we show that the surface potential in mixtures is well-described by an additive contribution of the electrochemical potential of each cation type, giving precise information on the surface charge mechanisms. We exploit this additive effect to demonstrate the selective layer-free measurements of four cations in blood serum, with performances equivalent to or beyond those of selective layer-based transistor ion sensors. Finally, we discuss the implications of these findings to various fields of research.

A 0D nanotransistor sensor that is chemically inert to pH

Ion-sensitive field-effect transistors (ISFETs) were initially developed with the aim of reducing the dimensions of glass electrodes (Fig. 1a,b) and thereby providing highly integrated and inexpensive biochemical sensors[31]. These devices have been further scaled for high-throughput sensing[32–34] and intracellular measurements[35], as well as to propose alternative sensing methods[36] (Fig. 1c). Devices in the present study are of nanometric dimensions[37,38] (Fig. 1d) and, therefore, are referred to as 0D ISFETs or 0D nanotransistor biosensors (see Methods and Supplementary Fig. 1). We integrated a large ISFET as a reference device together with the 0D ISFET on the same wafer. Although the two transistors were fabricated with identical processes, the oxides are not necessarily identical due to stress effects encountered during oxidation of the nanoscale structure[38–40]. When immersed in liquid, the 0D ISFET exhibited a U-shaped pH response, whereas the large ISFET showed the typical pH response for SiO_2, which was well-described by the SBM (Fig. 1e–h and Supplementary Figs. 2 and 3 for current–voltage curves and three other devices). The SBM can also describe the negligible pH sensitivity of the 0D ISFET in the pH 4–9 range, if one considers a reduced density of charged sites. This situation offers a unique opportunity to investigate ion-surface interactions by neglecting pH-mediated reactions.

Ion-specific effects and sensitivities beyond the Nernst limit

All experiments for salts in deionized (DI) water were performed at constant pH of ~5.5. For simplicity, we plot ψ_0^*, which represents the variation of ψ_0 with salt concentration ($\psi_0^* = 0$ at low ion concentration). The ψ_0^* responses for KCl/HCl, NaOH/NaCl

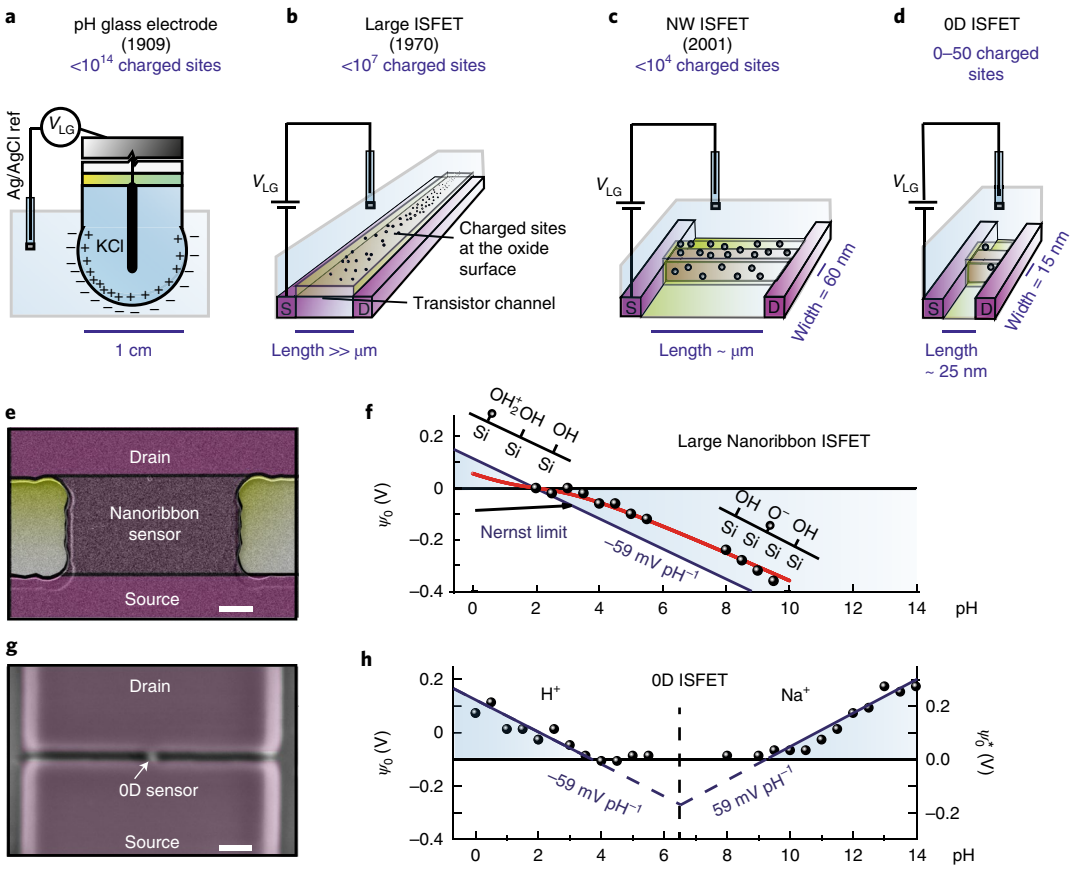

Fig. 1 | 0D ISFETs show negligible sensitivity to pH near neutral pH. a–d, Schematic view of a pH glass electrode (**a**), an ISFET (**b**), a nanowire (NW) ISFET (**c**) and a 0D ISFET (**d**) (see Methods for number of charged sites). **e**, Scanning electron microscope (SEM) image of a 40-nm-thick nanoribbon ISFET used as a reference device. Scale bar, 2 μm. **f**, Plot of ψ_0 versus pH for one nanoribbon ISFET (with NaOH and HCl). Black balls: experimental data points. Red line: theoretical fit with the SBM ($pK_a = +6$, $pK_b = -2$, the equilibrium constants for the deprotonation and the protonation reactions, respectively, and the total density of sites $= 5 \times 10^{18}\ m^{-2}$). Blue line: Nernst limit. Measured threshold voltages (V_{th}) were converted into $\psi_0 = V_{th}(PZC) - V_{th}$ (see Supplementary Fig. 2 for raw transistor characteristics and extraction of ψ_0). Drain voltage $V_d = 50$ mV. pH corresponding to the point of zero charge is PZC = 2, as is usual for SiO_2. **g**, SEM image of 0D ISFET. Scale bar, 100 nm. **h**, Plot of ψ_0 versus pH for one 0D ISFET (see Supplementary Fig. 2 for raw transistor characteristics and Supplementary Fig. 3 for three other 0D ISFETs). $V_d = 50$ mV. Solid black balls: experimental data points. Dark blue lines: Nernst limit. ψ_0^* is indicated on the right axis.

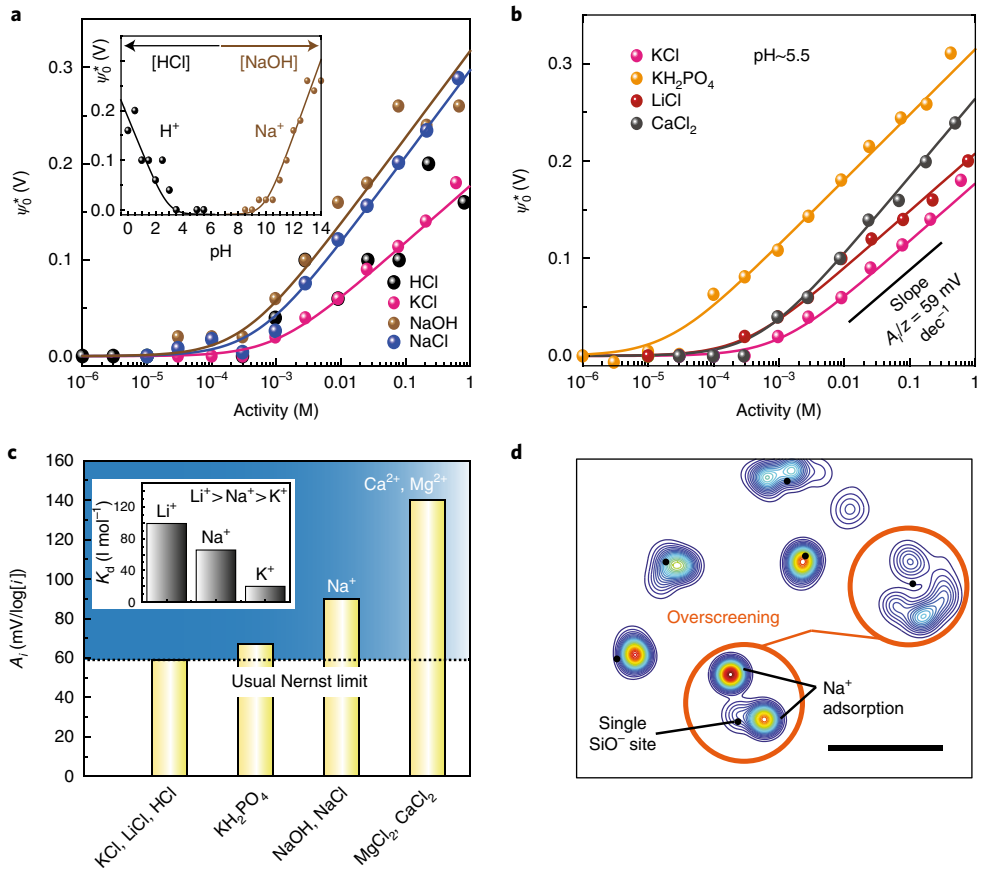

Fig. 2 | Signatures of ion-specific effects. a, ψ_0^* plotted as a function of cation activity for four different solutions (HCl, KCl, NaOH and NaCl) on a single 0D ISFET. Curves are fitted based on equation (1), which can be derived from an extended SBM (see Methods). **b**, ψ_0^* plotted as a function of cation activity for KCl, KH_2PO_4, LiCl and $CaCl_2$ on a single 0D ISFET. Curves are fitted based on equation (1). **c**, Parameter A_i obtained from fits with equation (1) for all studied solutions. The usual Nernst limit is shown as a reference. Inset: K_d, the association constant extracted from equation (7) (see Methods), reflects the degree of association of a given ion with the surface. K_d scales as the inverse of $[i_0]$. Extracted parameters as well as statistics over four devices are shown in Supplementary Table 1. **d**, Cation distribution at the interface obtained by MD simulation (averaged over 5 ns) for a solution of 0.3 M NaCl. This distribution represents the probability of the Na^+ position over the measurement period. The location of SiO^- sites is indicated by black points. Strength of colour (from blue to red) illustrates the stability of cation adsorption. Each charge site is compensated by at least one adsorbed cation. Additional ions due to overscreening (orange circle) are often located near a charge site. Horizontal scale bar, 1 nm.

(Fig. 2a) and various other monovalent and divalent salts (Fig. 2b) follow an increasing trend towards more positive values, suggesting cation adsorption at the surface. All curves fit a Nernst-like response well:

$$\psi_0^* = \psi_0 + \text{const} = (A_i/z_i)\log([i] + [i_0]) - (A_i/z_i)\log([i_0]) \quad (1)$$

where $[i_0]$ is an ion-specific constant that accounts for the plateau at low ion concentration, and A_i/z_i is the Nernst slope. The U-shaped pH response can be reproduced from equation (1) with $[i] = [H^+]$ at pH < 6 and $[i] = [Na^+]$ at pH > 6 (Fig. 2a, inset).

We found that $Li^+ > Na^+ > K^+$ (Fig. 2c, inset), corresponding to a reversed Hofmeister series. This series was previously obtained on silica by atomic force microscopy in liquid[41] and by MD[6]. As predicted by Shklovskii et al.[21], we found that the Nernst limit was overpassed for some ions. The Nernst slope A_i/z_i, which is important for sensor applications, is shown in Fig. 2b and compared in Fig. 2c. Estimates from Fig. 2a,b yield $59 \leq A_i \leq 140$ mV/log[i]. H^+, Li^+ and K^+ showed full Nernst sensitivity, Na^+ showed larger than Nernst sensitivity, and Ca^{2+} and Mg^{2+} demonstrated sensitivities more than twofold the Nernst sensitivity (see Supplementary Table 1 for statistics). We stress that ψ_0 was directly measured from the liquid gate without any amplification effect, and that A_i did not depend on ionic strength, as shown in the following for measurements in mixed solutions.

If we neglect pH-mediated ion adsorption, then a partially deprotonated silica surface is the most probable surface configuration to adsorb cations[17]. Recent MD simulations on such a surface predicted an ion-specific overscreening effect whose strength correlated with the experimentally obtained order for A_i (divalent ions $\gg Na^+ > K^+$)[6]. A direct link between overscreening and A_i can be derived analytically by introducing electrostatic correlations (as defined by the Frumkin isotherm[42,43]) in the Boltzmann ion distribution (see Methods and Supplementary Fig. 4). Our MD simulations for NaCl (0.3 M) on a partially deprotonated silica surface support the relevance of electrostatic correlations. From the time-averaged in-plane Na^+ distribution in the Stern layer, we found that two Na^+ ions could be located near the same SiO^- site (Fig. 2d and Supplementary Movie).

Additive effect on ψ_0

To gain additional insights into the underlying adsorption mechanism and from the perspective of a model for ψ_0 in complex solutions, we studied ψ_0^* in the presence of two potential-determining

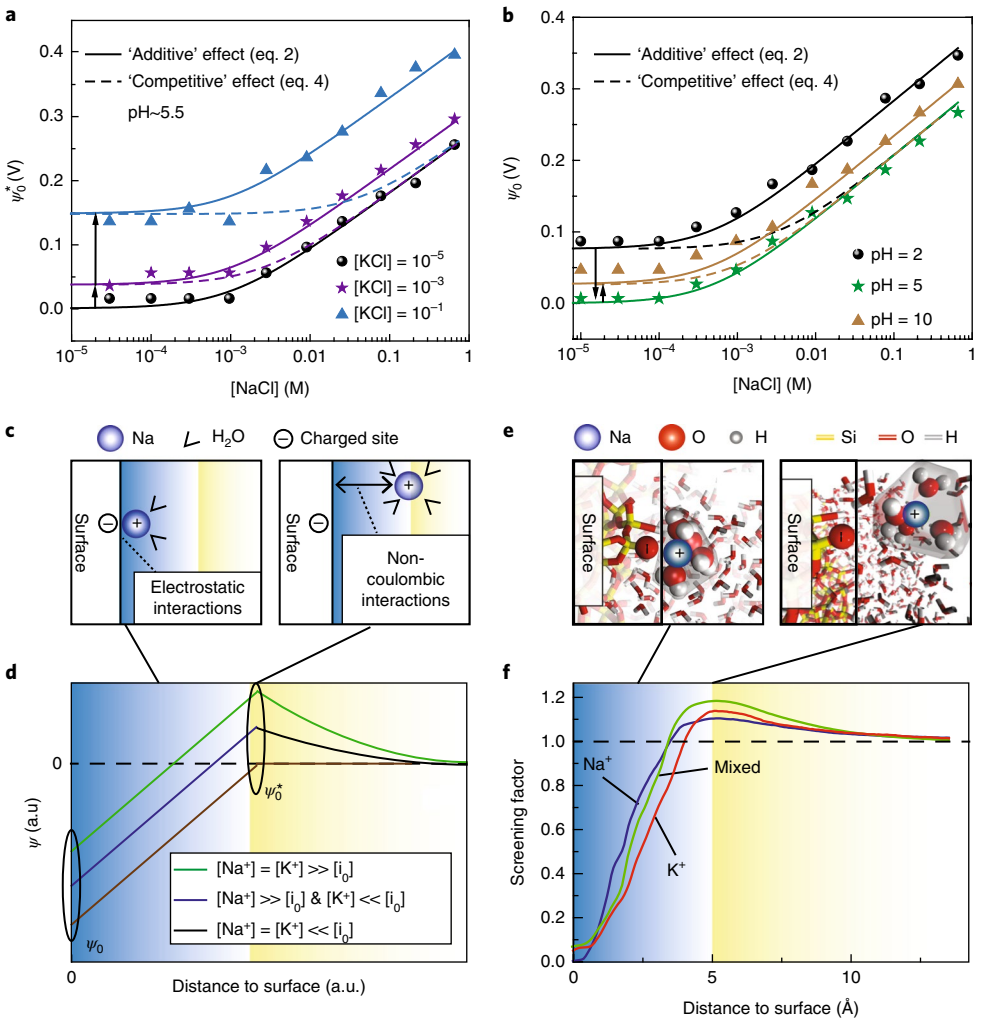

Fig. 3 | Additive contribution of multiple species on ψ_0. **a**, ψ_0^* versus [NaCl] at different [KCl] on one 0D ISFET. Experimental results are fitted with equation (2) with $A_i = 59$ mV for KCl, 90 mV for NaCl; $[i_0] = 5\times10^{-4}$ M for NaCl and 1×10^{-3} M for KCl. Dashed lines indicate expected results for a 'competitive' behaviour based on equation (4) (see Methods). **b**, Similar experiment as in **a**, for ψ_0 versus [NaCl] at different values of pH. Fits with equation (2) are obtained with $A_i = 59$ mV for HCl, 90 mV for NaCl and NaOH; $[i_0] = 5\times10^{-4}$ for NaCl, 5.3×10^{-4} for HCl and 1×10^{-4} M for NaOH. **c**, Schematic representation of the proposed model, which distinguishes between counterions located next to a charged site and ions adsorbed by non-Coulombic interactions. **d**, Schematic graph of ψ as a function of distance to the surface based on the proposed analytical model (see Methods) for different ion concentrations. Ions adsorbed by non-Coulombic interactions lead to overscreening and an 'additive' effect on the surface potential. **e**, Partially hydrated Na^+ ions simulated by MD are shown for two different distances from the surface. **f**, Screening factor determined by MD for NaCl (0.3 M), KCl (0.3 M) and mixed solutions.

ions. The ψ_0^* versus [NaCl] response at different [KCl] values is shown in Fig. 3a. Fits with equation (1) showed that A_i and $[i_0]$ were not affected by [KCl], but there was a tunable offset potential. Reasonable fits were obtained without adjustable parameters by considering an additive contribution of each cation type to ψ_0^*:

$$\psi_0^* = \text{const} + \sum_i \frac{A_i}{z_i} log\left([i] + [i_0]\right) \qquad (2)$$

This equation, which corresponds to the sum of the electrochemical potentials of the cations, with an ion-specific enhanced sensitivity as described previously (parameter A_i), was verified for the ψ_0 versus [NaCl] response at different pH values (Fig. 3b). Usual semi-empirical models such as the Nikolski–Eisenman equation do not lead to equation (2), because the presence of multiple species induces a competitive rather than an additive contribution to ψ_0 (refs. [7,29]; the most dominant species determines ψ_0 at equivalent association constants; Fig. 3a,b and Methods). A signature 'additive' effect has been reported previously by Tarasov and colleagues[7] when using silicon nanowire transistors covered with Al_2O_3. They discussed this effect on the basis of experimentally determined ψ_0 versus [KCl] at different pH values[7]. Suggesting that Cl^- ion adsorption is accompanied by proton release, those authors showed that a SBM with pH-mediated ion adsorption could account for the behaviour observed in their study. Unfortunately, this mechanism cannot be applied to the results shown in Fig. 3a because the pH sensitivity was negligible at pH ~5.5.

We suggest that 'additive' effects could occur without pH-mediated effects, and could be generalized to multiple species. On the basis of MD simulations and the Hofmeister-type behaviour, we consider ions to be non-punctual charges to account for hydration effects within the Stern layer. We assume that charges at the silica surface are mainly screened by counterions in the Stern layer, and that other

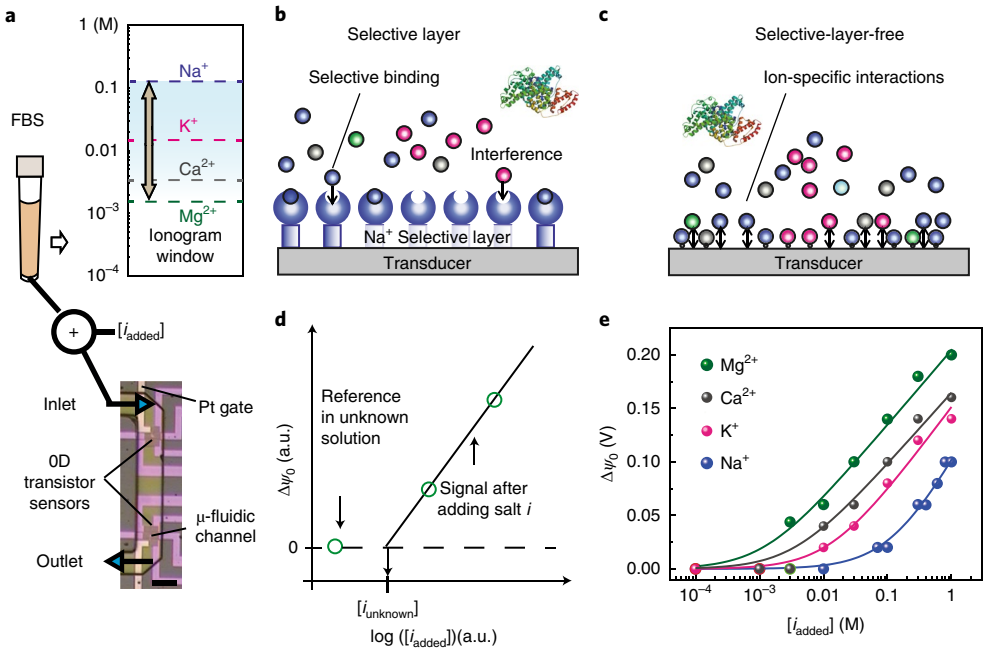

Fig. 4 | Selective-layer-free blood ionogram. a, Top, Schematic representations of the standard addition calibration method set-up and typical ion concentrations expected in FBS. Bottom, Optical top-view image of the device, the Pt electrode and the microfluidic channel. Scale bar, 100 μm. **b**, Schematic representation of an ion sensor with a selective layer that selectively captures a target ion. **c**, Schematic representation of the proposed versatile ion sensor device based on ion-specific interactions. **d**, Schematic graph representing expected $\Delta\psi_0$ measured with the standard addition calibration method. **e**, $\Delta\psi_0$ versus [] measured experimentally on a single device for FBS, where [] corresponds to $MgCl_2$, $CaCl_2$, KCl and NaCl concentrations. Curves are fitted with equation (3), and results are shown in Table 1. We report concentrations instead of activities for simplicity, because both representations give the same unknown ion concentrations.

ions interacting via non-Coulombic hydrophilic forces with silanol groups lead to an overscreening effect (Fig. 3c). This simplified picture of the modified Poisson–Boltzmann (MPB) equation reported in ref. [6] aims to capture the underlying mechanism, whereby ψ_0 is not only determined by the surface charge (density of deprotonated sites), but is also shifted by ψ_0^* due to ion accumulations at the Stern layer interface (Fig. 3d). This situation leads to an additive effect when both pH and ion concentration are tuned for pH-sensitive surfaces. Non-Coulombic forces at the origin of ψ_0^* can be described by an ion-specific potential of mean force (PMF_i)[6], which is the analogue of a material work function in semiconductor physics. Without significant ion–ion interactions between species, each ion species generates a built-in potential at the Stern layer interface, leading to equation (2) (see Methods). Additivity for multiple ion types is obtained in the model if ψ_0^* results only from non-Coulombic surface forces, when counterions fully screen the surface charge in the Stern layer. The proposed model is supported by MD analysis of the screening factor (a measure for the extent to which charges in the electrical double layer compensate for the bare surface charge) for Na^+, K^+ and a mixed solution (Fig. 3e,f and Supplementary Fig. 5).

Selective layer-free blood ionogram

To confirm the validity of equation (2) with a complex solution and to demonstrate a biomedical application based on ion-specific interactions, we used blood-derived fetal bovine serum (FBS, Life Technology; Fig. 4a). The usual approach for selectively measuring an ion of interest in a complex solution with miniaturized devices is to use an organic layer capable of trapping a target ion while minimizing the trapping of other ions (interferences). In that approach, each ion type requires a dedicated selective organic layer (Fig. 4b). Conversely, the additive effect reported above suggests the possibility of performing selective measurements without needing a selective layer (Fig. 4c). Strictly speaking, the ion-specific effects do not directly provide ion selectivity. However, combining ion-specific effects with the standard addition calibration method enables selective layer-free measurements. In this method, $\Delta\psi_0$ is measured after taking a reference potential in an unknown solution and spiking the unknown solution with an analyte of interest (ion *i*) with concentration $[i_{added}]$ (Fig. 4a,d). The related equation can be derived from equation (2):

Table 1 | Cation concentration extracted from the fits on all points of Fig. 4e with equation (3)

	Na^+ (mM)		K^+ (mM)		Ca^{2+} (mM)		Mg^{2+} (mM)	
	Fit	Range	Fit	Range	Fit	Range	Fit	Range
0D ISFET	135	117–153	13	11.7–14.3	3.5	2–5	1.2	1–1.4
Expected value	134	131–137	13.5	12.9–14.2	3.64	3.57–3.74	1.25	-

Results are compared with values provided by Life Technologies (including range), except for $[Mg^{2+}]$ (not provided by Life Technologies), which was analysed with a catalyst Dx biochemical analyser from Idexx. A_i = 108 mV for Na^+, 80 mV for K^+, 134 mV for Ca^{2+}, 140 mV for Mg^{2+}. The range is related to the standard deviation on $[i_{unknown}]$ from the fit on the measurements performed on one device at different ion concentrations.

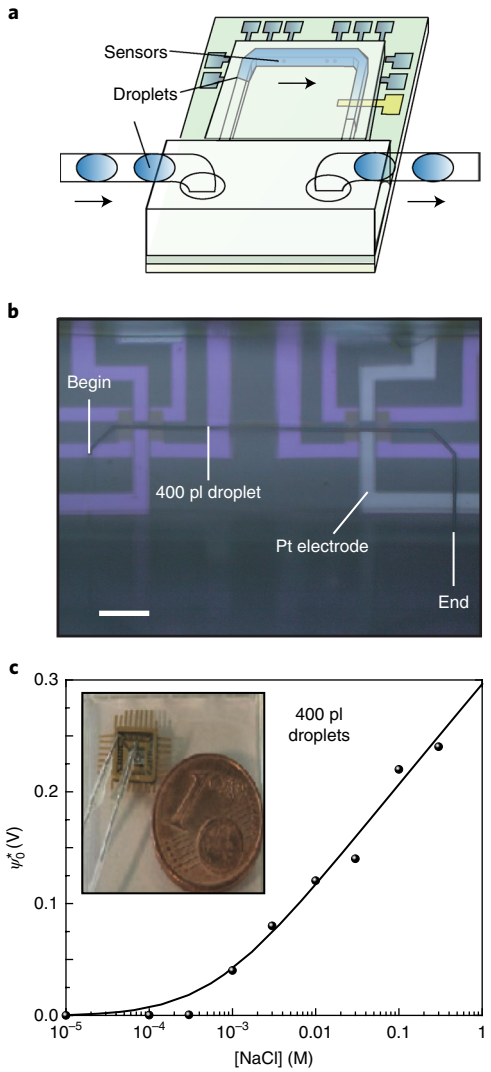

Fig. 5 | Subnanolitre sensing and high integration. a, Schematic representation of the microfluidic set-up for the demonstration of ion sensing in subnanolitre droplets (see Methods). The Pt electrode sets the droplet potential. **b**, Optical microscope image of the chip with a 10-μm-wide microfluidic channel filled with 400 pl DI water containing NaCl. Scale bar, 100 μm. **c**, Related droplet experiment for ψ_0^* versus [NaCl]. The fit was performed with equation (1). Inset, Image of the 1.5 mm × 1.5 mm lab-on-a chip with electrical contacts and tubes.

$$\begin{aligned}\Delta\psi_0(i_{\text{added}}) &= \psi_0(i_{\text{added}}) - \psi_0(0)\\ &= (A_i/z_i)\log([i_{\text{added}} + i_{\text{unknown}}] - \log[i_{\text{unknown}}])\end{aligned} \quad (3)$$

where $[i_{\text{unknown}}]$ is the unknown concentration for ion i, assuming $[i_0] \ll [i_{\text{unknown}}]$. In the case of a blood ionogram (detection of clinically relevant ions in blood), the worst situation in terms of interference is the detection of Mg^{2+}, because its concentration is two orders of magnitude lower than that of Na^+ (Fig. 4a). Mg^{2+} plays an important role in many enzymatic reactions, has an antitetany effect, and its concentration is important in the diagnosis of gastrointestinal disorders. $[Na^+]$ measurement is relevant for cardiac, renal and hepatic insufficiency, $[K^+]$ for cardiac arrhythmia and certain cancer treatments, and $[Ca^{2+}]$ for vitamin D deficiency, thyroid cancer, renal insufficiency and homeostasis. Experimental results for these four ions measured with a single 0D ISFET are shown in Fig. 4e. Cation concentrations extracted from the fits were within the expected data range (Table 1; see Supplementary Fig. 6 for another device with a different liquid-gate electrode). These results demonstrate that our device overcomes the two main challenges in creating a versatile ion sensor: (1) sensitivity to all cations of interest in a wide enough concentration range and (2) a low interference effect.

Discussion

The nanotransistors used in this study are very similar to those found in mobile phones and computers, without the metallic gate (the 14–22 nm FinFET node) (http://www.intel.com/content/www/us/en/silicon-innovations/intel-14nm-technology.html)[44]. A hybrid architecture combining digital microfluidics and nanotransistor sensors[45] could be an efficient way to automate the standard addition method, as these devices can efficiently sense ions in subnanolitre droplets (Fig. 5). The error obtained here with the selective-layer-free approach was the same or smaller than errors found for ions (other than H_3O^+) with selective-layer-based state-of-the-art nanowire[27,28] and graphene[46] transistor sensors or with a recently commercialized cheap, reusable (but not biocompatible) ion sensor for domestic purposes (see Supplementary Table 2 for a comparison with academic and commercial sensors). As the Nernst limit is usually not exceeded with selective-layer-based sensors, the 230% gain in sensitivity reported here for divalent ions strengthens the versatility of the sensor (Supplementary Note 1). A 0D ISFET can be seen as a model system to study and exploit ion-specific surface effects because it is more sensitive than typical ISFETs to ions in a wide concentration range[47]. Furthermore, the full theoretical ion sensitivity may be reached because the sensor is not degraded by pH sensitivity[29]. The dimensions of the device remain large compared to the Debye screening length (<1 nm in blood serum). The simplicity of equations (2) and (3) provides a route to compare results from a wide variety of systems (various oxides, emerging materials and biomolecules) and measurement techniques (atomic force microscopy[14,42], X-ray photoelectron spectroscopy[17], ISFETs[7,48], electrophoretic mobility[8,23]). Thus, studies on mixed solutions appear to contain substantial information on the ion–surface interaction mechanisms. Moreover, the results suggest that ion-specific effects may be implemented in biomolecular modelling software in the near future.

In conclusion, we have demonstrated a selective layer-free blood serum ionogram for Na^+, K^+, Ca^{2+} and Mg^{2+} based on nanotransistor technology. Substantial efforts and complexity would have been required to achieve the same results with a selective-layer approach. The present selective layer-free sensor is fully compatible with mass fabrication, versatile, reusable, label-free, biocompatible and miniaturized (1.5 mm × 1.5 mm lab-on-a-chip, including tubing and contacts). The sensor can operate when immersed in subnanolitre droplets. Selective-layer-free devices could have important clinical implications, particularly for individuals who undergo regular ionogram measurements (for hyperkalemy or renal insufficiency) or who take antidiabetic, corticoid or lithium medications.

This study offers perspectives to understand and tune the physicochemistry of (bio)-surfaces and an avenue of research for chemical sensors and biomedical engineering. Future systematic studies on aspects of the fabrication process (dimensions, oxidation temperature, annealing and so on) and materials (two-dimensional materials, various oxides and organic semiconductors) will enable tuning of the association constants and reduction of the low-frequency noise, thereby allowing application of this selective-layer-free approach to a wide variety of systems and complex chemical species.

Methods

Methods, including statements of data availability and any associated accession codes and references, are available at https://doi.org/10.1038/s41563-017-0016-y.

Received: 27 November 2016; Accepted: 22 December 2017;
Published online: 5 February 2018

References

1. Huebsch, N. & Mooney, D. Inspiration and application in the evolution of biomaterials. *Nature* **462**, 426–432 (2009).
2. Nel, A. E. et al. Underlying biophysicochemical interactions at the nano–bio interface. *Nat. Mater.* **8**, 543–548 (2009).
3. Someya, T., Bao, Z. & Malliaras, G. G. The rise of plastic bioelectronics. *Nature* **540**, 379–385 (2016).
4. Rembert, K. B. et al. Molecular mechanisms of ion-specific effects on proteins. *J. Am. Chem. Soc.* **134**, 10039–10046 (2012).
5. Salis, A. & Ninham, B. W. Models and mechanisms of Hofmeister effects in electrolyte solutions, and colloid and protein systems revisited. *Chem. Soc. Rev.* **43**, 7358–7377 (2014).
6. Hartkamp, R., Siboulet, B., Dufreche, J.-F. & Coasne, B. Ion-specific adsorption and electrosmosis in charged amorphous porous silica. *Phys. Chem. Chem. Phys.* **17**, 24683–24695 (2015).
7. Tarasov, A. et al. Understanding the electrolyte background for biochemical sensing with ion-sensitive field-effect transistors. *ACS Nano* **6**, 9291–9298 (2012).
8. Li, S. X., Guan, W., Weiner, B. & Reed, M. A. Direct observation of charge inversion in divalent nanofluidics devices. *Nano Lett.* **15**, 5046–5051 (2015).
9. Kenzaki, H. et al. Cafemol: a coarse-grained biomolecular simulator for simulating proteins at work. *J. Chem. Theor. Comput.* **7**, 1979–1989 (2011).
10. Snodin, B. E. K. et al. Introducing improved structural properties and salt dependence into a coarse-grained model of DNA. *J. Chem. Phys.* **142**, 234901 (2015).
11. Shoorideh, K. & Chui, C.-O. On the origin of enhanced sensitivity in nanoscale FET-based biosensors. *Proc. Natl. Acad. Sci. USA* **111**, 5111–5116 (2014).
12. Yates, D. E., Levine, S. & Healy, T. W. Site-binding model of the electrical double layer at the oxide/water interface. *Faraday Trans.* **70**, 1807–1818 (1974).
13. Van Hal, R. E. G., Eijkel, J. C. T. & Bergveld, P. A. General model to describe the electrostatic potential at electrolyte oxide interfaces. *Adv. Colloid Interface Sci.* **69**, 31–62 (1996).
14. Morag, J., Dishon, M. & Sivan, U. The governing role of surface hydration in ion specific adsorption to silica: an AFM-based account of the Hofmeister universality and its reversal. *Langmuir* **29**, 6317–6322 (2012).
15. Hocine, S. et al. How ion condensation occurs at a charged surface: a molecular dynamics investigation of the Stern layer for water–silica interfaces. *J. Phys. Chem. C.* **120**, 963–973 (2016).
16. Nostro, P. L. & Ninham, B. W. Hofmeister phenomena: an update on ion-specificity in biology. *Chem. Rev.* **112**, 2286–2322 (2012).
17. Shchukarev, A., Rosenqvist, J. & Sjöberg, S. XPS study of the silica–water interface. *J. Electron. Spectr. Rel. Phenom.* **137**, 171–176 (2004).
18. Criscenti, L.J., Cygan, R. T., Kooser, A.S. & Moffat, H.K. Water and halide adsorption to corrosion surfaces: molecular simulations of atmospheric interactions with aluminum oxyhydroxide and gold. *Chem. Mater.* **20**, 4682–4693 (2008).
19. Larson, I. & Attard, P. Surface charge of silver iodide and several metal oxides. Are all surfaces Nernstian? *J. Colloid Interface Sci.* **227**, 152–163 (2000).
20. Knopfmacher, O. et al. Nernst limit in dual-gated Si-nanowire FET sensors. *Nano Lett.* **10**, 2268–2274 (2010).
21. Shklovskii, B. I. Screening of a macroion by multivalent ions: correlation-induced inversion of charge. *Phys. Rev. E* **60**, 5802–5811 (1999).
22. Grosberg, A. Yu., Nguyen, T. T. & Shklovskii, B. I. Colloquium: the physics of charge inversion in chemical and biological systems. *Rev. Mod. Phys.* **74**, 329–345 (2002).
23. Martin-Molina, A., Rodriguez-Beas, C. & Faraudo, J. Charge reversal in anionic liposomes: experimental demonstration and molecular origin. *Phys. Rev. Lett.* **104**, 168103 (2010).
24. Pinna, M.C., Salis, A., Monduzzi, M. & Ninham, B.W. Hofmeister series: the hydrolytic activity of aspergillus niger lipase depends on specific anion effects. *J. Phys. Chem. B* **109**, 5406–5408 (2005).
25. Jung, W., Han, J. & Ahn, C. H. Point-of-care testing (POCT) diagnostic systems using microfluidic lab-on-chip technologies. *Microelectron. Eng.* **132**, 46–57 (2015).
26. Bühlmann, P., Pretsch, E. & Bakker, E. Carrier-based ion-selective electrodes and bulk optodes. 2. Ionophores for potentiometric and optical sensors. *Chem. Rev.* **98**, 1593–1688 (1998).
27. Cao, A. et al. Ionophore-containing siloprene membrane: direct comparison between conventional ion-selective electrodes and silicon nanowire-based field-effect transistors. *Anal. Chem.* **87**, 1173–1179 (2015).
28. Wipf, M. et al. Selective sodium sensing with gold-coated silicon nanowire field-effect transistors in a differential setup. *ACS Nano* **7**, 5978–5983 (2013).
29. Accasteli, E. et al. Multi-wire tri-gate silicon nanowires reaching milli-pH unit resolution in one micron square footprint. *Biosensors* **6**, 9–15 (2016).
30. Stoop, R. L. et al. Competing surface reactions limiting the performance of ion-sensitive field-effect transistors. *Sens. Actuat. B* **220**, 500–507 (2015).
31. Bergveld, P. Development of an ion-sensitive solid-state device for neurophysiological measurements. *IEEE Trans. Biomed. Eng.* **17**, 70–71 (1970).
32. Cui, Y., Wei, Q., Park, H. & Lieber, C. M. Nanowire nanosensors for highly sensitive and selective detection of biological and chemical species. *Science* **293**, 1289–1292 (2001).
33. Stern, E. et al. Label-free immunodetection with CMOS-compatible semiconducting nanowires. *Nature* **445**, 519–522 (2007).
34. Rothberg, J. M. et al. An integrated semiconductor device enabling non-optival genome sequencing. *Nature* **475**, 348–352 (2011).
35. Tian, B. et al. Three-dimensional, flexible nanoscale field-effect transistors as localized bioprobes. *Science* **329**, 830–834 (2010).
36. Li, J. et al. Sensitivity enhancement of Si nanowire field-effect transistor biosensors using single trap phenomena. *Nano Lett.* **14**, 3504–3509 (2014).
37. Clement, N. et al. A silicon nanowire ion-sensitive field-effect transistor with elementary charge sensitivity. *Appl. Phys. Lett.* **98**, 014104 (2011).
38. Takahashi, Y. et al. Fabrication technique for Si single-electron transistor operating at room temperature. *Electron. Lett.* **31**, 136–137 (1995).
39. Uematsu, M. et al. Two-dimensional simulation of pattern-dependent oxidation of silicon nanostructures on silicon-on-insulator substrates. *Solid-State Electron.* **48**, 1073–1078 (2004).
40. Han, X.-L. et al. Modelling and engineering of stress-based controlled oxidation effects for silicon nanostructure patterning. *Nanotechnology* **24**, 495301 (2013).
41. Morag, J., Dishon, M. & Sivan, U. The governing role of surface hydration in ion specific adsorption to silica: an AFM-based account of the Hofmeister universality and its reversal. *Langmuir* **29**, 6317–6322 (2012).
42. Ricci, M., Spijker, P. & Voitchovsky, K. Water-induced correlation between single ions imaged at the solid–liquid interface. *Nat. Commun.* **5**, 4400 (2014).
43. Trasobares, J. et al Estimation of π–π electronic couplings from current measurements. *Nano Lett.* **17**, 3215–3224 (2017).
44. Rigante, S. et al. Sensing with advanced computing technology: fin field-effect transistors with high-*k* gate stack on bulk silicon. *ACS Nano* **9**, 4872–4991 (2015).
45. Schutt, J. et al. Compact nanowire sensors probe microdroplets. *Nano Lett.* **16**, 4991–5000 (2016).
46. Wang, C. et al. A label-free and portable graphene FET aptasensor for children blood lead detection. *Sci. Rep.* **6**, 21711 (2016).
47. Knopmacher, O. et al. Silicon-based ion-sensitive field-effect transistor shows negligible dependence on salt concentration at constant pH. *Chem. Phys. Chem.* **13**, 1157–1160 (2012).
48. Parizi, K. B., Xu, X., Pal, A., Hu, X. & Wong, H. S. P. ISFET pH sensitivity: counter-ions play a key role. *Sci. Rep.* **7**, 41305 (2017).

Acknowledgements

The authors thank M. Clément at 'Clinique Vétérinaire du Clair Matin' for performing the ionogram for [Mg^{2+}], S. Frickey for discussions on the use of ionograms in the medical environment, Y. Coffinier for providing FBS and for discussions, and P. Joseph for advice on microfluidic chips. The authors also thank B. Coasne for assistance regarding MD and for discussions, and A. Shuchukarev, F. Alibart, A. Charrier, P. Temple-Boyer, A.M. Gué, C. Bergaud, L. Nicu, A. Bancaud, G. Larrieu, D. Vuillaume, D. Guérin, S. Lenfant and I. Mahboob for their feedback on the manuscript. This study was funded by Singlemol and BQR projects from the Nord-Pas de Calais Council, Lille University and NTT.

Author contributions

R.S. fabricated the lab-on-a-chip, prepared solutions, performed electrical measurements and analysed the data. R.H., B.S. and J.-F.D. performed MD simulations. R.H. addressed overscreening and mixed electrolyte issues by MD and provided careful feedback on the manuscript. J.-F.D. derived equations (6) and (7) and wrote the related program. K.N. fabricated the silicon nanotransistors. A.F. continuously gave input on the study process and the manuscript. All authors discussed the results. N.C supervised the study, analysed the data, proposed the models for large slopes and additive effects, and wrote the paper.

Competing interests

The authors declare no competing financial interests.

Additional information

Supplementary information accompanies this paper at https://doi.org/10.1038/s41563-017-0016-y.

Reprints and permissions information is available at www.nature.com/reprints.

Correspondence and requests for materials should be addressed to N.C.

Publisher's note: Springer Nature remains neutral with regard to jurisdictional claims in published maps and institutional affiliations.

Methods

Equations. *Semi-empirical Nikolski–Eisenman equation.* The semi-empirical Nikolski–Eisenman equation was used to study interference issues in ion sensing, in particular to describe the ion-exchange mechanism in ion-selective electrodes.

$$\psi_0 = \text{const} + A\log\left([i] + \sum_j k_{ij}[j]\right) \quad (4)$$

where k_{ij} is the selectivity coefficient and A is the Nernst slope (for monovalent ions). k_{ij}=1 corresponds to the absence of selective membrane and to a full sensitivity to all cations. Equation (4) cannot reproduce the results shown in Fig. 3a,b.

Analytical model for ψ_0. We consider there to be non-punctual ions and non-Coulombic ion–surface interactions, and further suppose that all charged surface sites are fully screened by counterions in the Stern layer (Fig. 3e). As a result,

$$\psi_0(\text{pH}, [i]) = f(\text{pH}) + \psi_0^*[i] \quad (5)$$

f(pH) is related to the density of protonated/deprotonated sites as described by the usual SBM[13]. The left part of the U-shaped curve could be either related to f(pH) or $\psi_0^*[i]$ (non-Coulombic cation–surface interactions).

$\psi_0^*[i]$ is related to non-Coulombic ion-specific interactions, whose strength is determined by $U_{\text{PMF}i}$, which is the analogue of a work function in semiconductor physics. Therefore, ψ_0^* can be regarded as a built-in potential in Schottky or pn diodes, with a potential drop at interfaces determined by $U_{\text{PMF}i}$ and the ion concentration in bulk. As each ion type has its own $U_{\text{PMF}i}$, each ion distribution should be governed by a pseudo-Fermi potential. In other words, if the non-Coulombic interactions between one ion type and the surface do not depend on the presence of other species, then each ψ_{0i}^* should follow the variations in the electrochemical potential of species i and contribute additively to the measured ψ_0^* (equation (2)). The additive contribution is qualitatively supported by MD. In the case that surface sites are weakly screened by counterions, competitive effects should be observed.

$\psi_0^*[i]$ and the Hofmeister effect could in principle be related to $U_{\text{PMF}i}$ via association constants for a single ion species. Theoretically, the potential of mean force $U_{\text{PMF}i}$ (Supplementary Fig. 5b) can be related to a Bjerrum-like association constant:

$$K_d(d) = \int_0^d \mathrm{d}r 2\pi r^2 \mathrm{e}^{-\beta U_{\text{PMF}_i}(r)} \quad (6)$$

where $\beta = 1/kT$, and d and r are distances from the surface. In the case of a single ion species, a SBM could be applied to describe ψ_0^* (equations (7)–(9)).

$$C_d \frac{kT}{zq}\ln(x) = -\frac{qK_dN_s[i]x}{1+K_d[i]x} \quad (7)$$

with

$$x = e^{[(1-\alpha)(-zq\psi_0^*/kT)]} \quad (8)$$

and

$$\alpha = \frac{2g\Phi C_d}{z^2q^2N_s}kT \quad (9)$$

For simplicity, we consider N_s to be the density of interacting sites (silanol groups), considering that each ion adsorbed from the non-Coulombic forces does not interact with a single silanol site and that non-Coulombic interactions exist with charged sites. Best fits are obtained by considering a constant capacitance C_d (Supplementary Fig. 4a). This capacitance may be dominated by the few-ångstroms-thick layer between the minimum in $U_{\text{PMF}i}$ and $U_{\text{PMF}i} \approx 0$ in Supplementary Fig. 5b, where ions are still not completely free to move. We used $C_d \approx 0.2\,\text{F m}^{-2}$ based on additional experiments (reported in a subsequent paper). If C_d is considered to be only the diffuse layer capacitance, the Grahame equation can be used and equation (7) can be solved by the Newton–Raphson method (Supplementary Fig. 4b). C_d can be considered constant in the blood ionogram experiment due to the large concentrations of Na^+ and Cl^-. An ion–ion attraction parameter α, related to the overscreening effect, can be introduced to account for slopes beyond the Nernst limit. $\alpha = 0$ leads to the Nernst response and $\alpha > 0$ (ion–ion attraction) enables a distribution steeper than the Nernst distribution. g is an interaction constant defined by the Frumkin isotherm[43] and Φ is a segregation constant[49] that accounts for ion–ion interactions. K_d values obtained from MD with equation (6) follow the same trend as K_d values obtained from experimental data with equation (7) (Supplementary Table 1) if 0.2 SiOH sites per nm^2 are considered. K_d is expected to strongly depend on surface specifics (various site densities, effective charge sites, and so on (Hocine et al., in preparation)). Equation (7) can reproduce the additive effect if C_d is considered constant (linear effect). The potential across C_d arises from the sum of trapped (adsorbed) charges from each ion type generated by non-Coulombic interactions (each ion type generates ψ_{0i}^*). Counterions face competitive adsorption in the Stern layer due to strong electrostatic forces (Supplementary Fig. 5c), but this fact does not impact the model for ψ_0^*.

Number of charged sites on the nanoscale transistor estimated by the SBM. The SiO_2 sensing area is $\sim 2.75 \times 10^{-15}\,\text{m}^2$, which typically corresponds to thousands of SiOH groups. In terms of non-Coulombic interactions, this number is sufficiently large for the proposed model to be applicable. However, the number of deprotonated bonds may be relatively small, especially if the density of SiOH groups is reduced. This possibility could explain our observations of fluctuations in the pH response data, the negligible pH response over a wide pH range due to the saturation of SiO^- bonds, and the U-shaped pH response (non-Coulombic interactions depend to a lesser extent on the density of SiO^- bonds). More quantitatively, a very weak pH response is obtained with the SBM, considering a density of less than 1×10^{16} charged sites per m^2 (<50 charged sites).

Device fabrication. *Silicon nanodevice.* The undoped silicon nanochannel was oxidized (1,100 °C dry thermal oxidation) to form a 35-nm-thick high-quality oxide, leading to very stable nanodevices[50,51]. Most of the nanoscale devices had no oxide traps, as confirmed by the absence of a random telegraph signal[52]. In liquid, we did not notice any leakage or erratic behaviour of the nanoscale device during months of experiments, in contrast to some previous reports of transistors in liquid with a silicon dioxide interface[53].

The 0D and nanoribbon transistors were fabricated on a silicon-on-insulator (SOI) wafer. For the nanoscale transistor, a narrow constriction sandwiched between two wider (400-nm-wide) channels was first patterned on the 30-nm-thick top silicon layer (p-type, boron concentration of $1 \times 10^{15}\,\text{cm}^{-3}$). The length and width of the constriction channel were 30 and 40 nm, respectively. No constriction was defined for the nanoribbon transistor. The patterning was followed by thermal oxidation at 1,100 °C to form a 35-nm-thick SiO_2 layer around the channel. This oxidation process reduced the size of the constriction to $\sim 15 \times 25\,\text{nm}^2$. Phosphorus ions were then implanted 5 µm away from the constriction using a resist mask to form highly doped source and drain regions. Finally, aluminium electrodes were evaporated on the source and drain regions.

Lab-on-a-chip. The polydimethylsiloxane (PDMS)-based lab-on-a-chip is highly miniaturized (1.5 mm × 1.5 mm, including access tubes and electrical contacts). The alignment protocol is described in ref. [54]. We considered 200 µm to be the optimum distance between the sensors and the electrical contacts to achieve high integration and a reliable lab-on-a-chip without leakage. Figures 1–3 were obtained using an Ag/AgCl electrode ('Electrical measurements' section). For the blood serum and subnanolitre droplets, we used an 'on-chip' Pt electrode instead of the Ag/AgCl electrode to obtain an ionogram lab-on-a-chip with high integration (Figs. 4a and 5c inset). We did not notice relevant differences from the Ag/AgCl electrode (Supplementary Fig. 6).

Picolitre-range droplets in microfluidic channels. We developed a simple methodology to handle picolitre volumes of analytes inside the microfluidic system with a 10 µm channel width. Discrete volumes of analyte were manually drawn into the polytetrafluoroethylene (PTFE) tube (0.7 mm/0.3 mm outer/inner diameter) with a syringe pump at 0.1 µl min^{-1}. Liquid flow was monitored continuously under an optical microscope. Liquid volume was calculated by considering the length of the droplet inside the channel (~920 µm in Fig. 5b) and the channel dimensions (44 µm × 10 µm). Once the desired droplet with known volume had covered the entire device for I–V measurements, the inlet pressure was released to avoid further movement of the liquid droplet inside the channel.

Solution preparation. Solutions with different ion concentrations were prepared in DI water (resistivity 18 MΩ). Salts (NaCl, KCl, KH_2PO_4, $MgCl_2$ and $CaCl_2$) with purity >99% were purchased from Fluka Analytical, Alfa Aesar, Sigma Aldrich or Analyticals Carlo Erba. The pH of salt in the DI water was ~5.5, as expected considering the diffusion of CO_2 into water. Standard FBS was purchased from Life Technologies. Provided ion concentrations for Na^+, K^+ and Ca^{2+} are reported in Table 1. The ion concentration for Mg^{2+} was estimated with a catalyst Dx biochemical analyser from Idexx. The same protocol as used for DI water was used to prepare tubes of FBS with various ion concentrations.

Electrical measurements. For electrical measurements, a commercial Ag/AgCl electrode (RE-1B: diameter 6 mm, EL-A-008 electrolytic bridge; Biologic SAS) was inserted in an electrochemical cell for flat materials (A-011951 from Biologic SAS) at the end of the microfluidic tube, and used as the liquid gate (Supplementary Fig. 7). The temperature in the electrical measurements room was controlled at 293 K. Electrical measurements were performed with a Keithley 4200 SCS parameter analyser. Electrical measurements were performed first for the most dilute solution, after which the ion concentration was increased. At each switching of sample solution, the inlet tube was rinsed with DI water and blown dry with

nitrogen. The solutions were transported by a syringe pump (KD Scientific) with manually controlled constant flow rate of 10 µl min^{-1}. The pump was stopped during measurements. Threshold voltages V_{th} were converted into surface potential via $\psi_0 = V_{th}(PZC) - V_{th}$, and taken from I_d–V_g in the reverse bias sweep. Concentration can be related to activity using the free ion activity coefficient γ, where $[a] = \gamma(c)$, with site interaction theory (SIT). The value of γ depends on the concentration of ions and charge in the solution, the charge of the ion and the diameter of the ion (http://www.lenntech.com/calculators/activity/activity-coefficient.htm).

MD simulations. The MD simulations followed the protocol detailed in ref. [55]. In brief, amorphous silica was created by annealing and quenching a silica melt. This resulted in bulk silica with structure factor and density in good agreement with experimental results. A surface was created by cutting the silica and then removing uncoordinated Si atoms, as well as O atoms that were no longer connected to any Si atom. This left dangling O atoms, which were saturated with H atoms to form charge-neutral silanol groups. The silica surface contained 64 silanol groups spread over an area of 35.8 Å × 35.8 Å, in agreement with experimentally measured silanol densities. We deprotonated eight silanol sites to create a surface charge density of −0.1 C m^{-2}. A channel was formed by two dissimilar, parallel walls, ~4 nm apart. MD simulations were performed using large-scale atomic/molecular massively parallel (LAMMPS) with a simulation time step of 1 fs. For the Supplementary Movie, visualization was performed with visual molecular dynamics (VMD) software.

Statistics. *Fluctuations on a single device.* For each device, ψ_0 was typically measured with 10 different solutions corresponding to different added concentrations, each reported point being an individual value. Standard deviations from fits with equations (1) and (3) are shown in Supplementary Table 1 and Table 1. A total of 100 repeated measurements of the threshold voltage, representing fluctuations of ψ_0 in repeated measurements, are shown in Supplementary Fig. 8. In that experiment, after each measurement, the flow of solution in the microfluidic channel was turned on for few minutes at 1 µl min^{-1} and stopped before the next measurement. The standard deviation was ~10 mV for all solutions.

Device-to-device fluctuation. For studies of ions in DI water, four devices were measured simultaneously for all different tested solutions, and experimental points shown in this Article are those of a representative device. Statistical results for A_i and $[i_0]$ are shown in Supplementary Table 1. No data were removed from the statistics. A reproducibility test for the U-shaped pH response was performed on another chip and included in the statistics of NaOH and HCl in Supplementary Table 1.

For the blood ionogram experiment, four devices were also measured simultaneously. The results shown in Fig. 4e correspond to the device with the lowest standard deviation. Statistics for the four devices are shown in Supplementary Table 3. No data were removed from the statistics. The blood ionogram experiment was reproduced with another device taken from another part of the silicon wafer with an additionally prepared PDMS lab-on-a-chip and solutions from another FBS bottle. In that test, an Ag/AgCl electrode was also used instead of a Pt electrode. Results for this experiment are shown in Supplementary Fig. 6.

Life Sciences Reporting Summary. Further information on experimental design is available in the Life Sciences Reporting Summary.

Code availability. Codes related to the SBM, equations (1) to (9) and MD simulations are available upon request.

Ethical regulation statement. FBS is authorized by the CNRS Ethics Comittee.

Data availability. Data supporting the findings of this study are available within the article (and its Supplementary Information) and from the corresponding author upon reasonable request.

References

49. Aleveque, O. et al. Electroactive self-assembled monolayers: Laviron's interaction model extended to non-random distribution of redox centers. *Electrochem. Commun.* **12**, 1462–1466 (2010).
50. Yamahata, G., Giblin, S. P., Kataoka, M., Karasawa, T. & Fujiwara, A. Gigahertz single-electron pumping in silicon with an accuracy better than 9.2 parts in 10^7. *Appl. Phys. Lett.* **109**, 013101 (2016).
51. Chida, K., Desai, S., Nishiguchi, K. & Fujiwara, A. Power generation by Maxwell's demon. *Nat. Commun.* **8**, 15310 (2017).
52. Clement, N., Nishiguchi, K., Fujiwara, A. & Vuillaume, D. One-by-one trap activation in silicon nanowire transistors. *Nat. Commun.* **1**, 92 (2010).
53. Tarasov, A. et al. Understanding the electrolyte background for biochemical sensing with ion-sensitive field-effect transistors. *ACS Nano* **6**, 9291–9298 (2012).
54. Sivakumarasamy, R. et al A simple and inexpensive technique for PDMS/silicon chip alignment with sub-µm alignment. *Anal. Methods* **6**, 97–101 (2014).
55. Hartkamp, R., Siboulet, B., Dufreche, J.-F. & Coasne, B. Ion-specific adsorption and electrosmosis in charged amorphous porous silica. *Phys. Chem. Chem. Phys.* **17**, 24683–24695 (2015).

nature research

Corresponding author(s): Nicolas Clement

☐ Initial submission ☐ Revised version ☒ Final submission

Life Sciences Reporting Summary

Nature Research wishes to improve the reproducibility of the work that we publish. This form is intended for publication with all accepted life science papers and provides structure for consistency and transparency in reporting. Every life science submission will use this form; some list items might not apply to an individual manuscript, but all fields must be completed for clarity.

For further information on the points included in this form, see Reporting Life Sciences Research. For further information on Nature Research policies, including our data availability policy, see Authors & Referees and the Editorial Policy Checklist.

Experimental design

1. Sample size

   Describe how sample size was determined.

   For the Blood Ionogram experiment, we used a standard commercial Fetal Bovine Serum (FBS) from Life Technologies for this proof of concept. FBS can be considered as a "model" solution. From the same mother bottle of 100 mL, we have prepared various tubes with added salts (in solid state). Each point on the blood ionogram experiment corresponds to the solution related to 1 tube with a given added salt concentration. The measurements has been performed simultaneously with 4 devices whose results are shown in SI.

2. Data exclusions

   Describe any data exclusions.

   No data were excluded from the analysis.

3. Replication

   Describe whether the experimental findings were reliably reproduced.

   The experiment shown in the main paper has been fully replicated using a different FBS bottle, a different silicon chip taken from another part of the wafer, a new PDMS microfluidic channel, and using an Ag/AgCl electrode instead of a Pt electrode (see SI).

4. Randomization

   Describe how samples/organisms/participants were allocated into experimental groups.

   No randomization is applied for FBS.

5. Blinding

   Describe whether the investigators were blinded to group allocation during data collection and/or analysis.

   No randomization is applied for FBS.

Note: all studies involving animals and/or human research participants must disclose whether blinding and randomization were used.

6. Statistical parameters

For all figures and tables that use statistical methods, confirm that the following items are present in relevant figure legends (or in the Methods section if additional space is needed).

n/a	Confirmed
☐	☒ The exact sample size (*n*) for each experimental group/condition, given as a discrete number and unit of measurement (animals, litters, cultures, etc.)
☐	☒ A description of how samples were collected, noting whether measurements were taken from distinct samples or whether the same sample was measured repeatedly
☐	☒ A statement indicating how many times each experiment was replicated
☐	☒ The statistical test(s) used and whether they are one- or two-sided (note: only common tests should be described solely by name; more complex techniques should be described in the Methods section)
☐	☒ A description of any assumptions or corrections, such as an adjustment for multiple comparisons
☐	☒ The test results (e.g. *P* values) given as exact values whenever possible and with confidence intervals noted
☐	☒ A clear description of statistics including central tendency (e.g. median, mean) and variation (e.g. standard deviation, interquartile range)
☐	☒ Clearly defined error bars

See the web collection on statistics for biologists for further resources and guidance.

Software

Policy information about availability of computer code

7. Software

Describe the software used to analyze the data in this study.	For data point analysis, we used Origin Software v7.5 (originlab). For the MD simulations, we used a script implemented into LAMMPS.

For manuscripts utilizing custom algorithms or software that are central to the paper but not yet described in the published literature, software must be made available to editors and reviewers upon request. We strongly encourage code deposition in a community repository (e.g. GitHub). *Nature Methods* guidance for providing algorithms and software for publication provides further information on this topic.

Materials and reagents

Policy information about availability of materials

8. Materials availability

Indicate whether there are restrictions on availability of unique materials or if these materials are only available for distribution by a for-profit company.	FBS is available commercially from Life Science.

9. Antibodies

Describe the antibodies used and how they were validated for use in the system under study (i.e. assay and species).	No antibodies were used.

10. Eukaryotic cell lines

a. State the source of each eukaryotic cell line used.	No eukariotic cells were used.
b. Describe the method of cell line authentication used.	No eukariotic cell lines were used.
c. Report whether the cell lines were tested for mycoplasma contamination.	No eukariotic cell lines were used.
d. If any of the cell lines used are listed in the database of commonly misidentified cell lines maintained by ICLAC, provide a scientific rationale for their use.	No commonly misidentified cell lines were used.

Animals and human research participants

Policy information about studies involving animals; when reporting animal research, follow the ARRIVE guidelines

11. Description of research animals

Provide details on animals and/or animal-derived materials used in the study.	Standard Fetal Bovine Serum was purchased from Life Technologies.

Policy information about studies involving human research participants

12. Description of human research participants

Describe the covariate-relevant population characteristics of the human research participants.	This study did not involve human research participants.